JOURNAL OF GEOPHYSICAL RESEARCH: OCEANS, VOL. 118, 1–10, doi:10.1002/2013JC009341, 2013

Nonseasonal fluctuations of the Arctic Ocean mass observed by the GRACE satellites

Denis L. Volkov[1] and Felix W. Landerer[2]

Received 12 August 2013; revised 5 November 2013; accepted 6 November 2013.

[1] Time variable gravity observations from the GRACE satellites reveal strong nonseasonal fluctuations of bottom pressure in the Arctic Ocean on the time scales from 2 to 6 months and a record-high bottom pressure anomaly in February of 2011. Here, we examine the nature and driving forces behind those fluctuations. We find that the nonseasonal variability of the Arctic Ocean mass is strongly coupled to wind forcing. The zonal wind pattern is correlated with a dipole pattern of Arctic Ocean mass changes. Westerly wind intensification over the North Atlantic at about 60°N as well as over the Russian Arctic continental shelf break cause the ocean mass to decrease in the Nordic seas and in the central Arctic, and to increase over the Russian Arctic shelf. Basin-wide Arctic Ocean mass fluctuations are correlated with northward wind anomalies over the northeastern North Atlantic and Nordic seas, and over the Bering Sea. We show that positive (negative) Arctic Ocean mass anomalies are associated with anticyclonic (cyclonic) anomalies of the large-scale ocean circulation pattern. Based on ocean model simulations, we conclude that the observed nonseasonal Arctic Ocean mass variability is mostly explained by the net horizontal wind-driven transports, and the contribution of fresh water fluxes is negligible. We demonstrate that transport anomalies across both the Atlantic and Pacific gateways were equally important for generating large Arctic Ocean mass anomalies in 2011.

Citation: Volkov, D. L., and F. W. Landerer (2013), Nonseasonal fluctuations of the Arctic Ocean mass observed by the GRACE satellites, *J. Geophys. Res. Oceans*, *118*, doi:10.1002/2013JC009341.

1. Introduction

[2] Continuous monitoring of the Arctic Ocean sea surface height (SSH) with satellite altimetry is inhibited by sea ice. Several recent studies used altimetry and hydrographic data to examine the variability of sea level in the ice-free sub-Arctic regions [e.g., *Mork and Skagseth*, 2005; *Steele and Ermold*, 2007; *Volkov and Pujol*, 2012; *Volkov et al.*, 2013a, 2013b]. Tide gauges have been used to study coastal Arctic Ocean sea level [*Proshutinsky et al.*, 2004, 2007; *Richter et al.*, 2012; *Calafat et al.*, 2013], but only a few gauges have sufficiently long records over the last two decades and their geographical distribution is uneven.

[3] Nontidal sea level variability is due to (i) changes in thermohaline properties of seawater (steric changes) from variations in buoyancy fluxes and heat and salt advection

column, caused by the wind-driven redistribution of water within the ocean and the exchange of water between the ocean, atmosphere, and land. Several bottom pressure recorders have been used to study the mass-related component of sea level variability in the central Arctic [e.g., *Morison et al.*, 2006; *Peralta-Ferriz et al.*, 2011]. While there is no continuous, basin-wide monitoring of the steric component of the Arctic Ocean SSH, the Gravity Recovery and Climate Experiment (GRACE, *Tapley et al.* [2004]) satellite mission has been providing observations of the monthly ocean mass (OcM) variations since 2002.

[4] It has been shown that GRACE can reliably observe Arctic OcM changes. Good agreement between GRACE OcM and in situ bottom pressure recorders has been found near the North Pole, in the Beaufort Sea, and in the Fram Strait (just west of Spitsbergen) [*Morison et al.*, 2006; *Per-*

[5] In February 2011, GRACE observed a record-high anomaly of the Arctic OcM with a peak magnitude exceeding 4 cm above the 2003–2012 average. Here, we analyze the nonseasonal variability of the Arctic OcM, obtained by subtracting the monthly mean climatology from monthly GRACE measurements. Thus, our study is mostly focused on GRACE signals with periods from 2 to about 6 months that dominate the nonseasonal variability of the Arctic OcM. We investigate the driving mechanisms for the observed nonseasonal fluctuations. In particular, we evaluate the relative contributions of wind forcing and fresh water fluxes and identify the sources that contributed to the record-high Arctic OcM anomaly in February 2011.

[6] A recent study by *Landerer and Volkov* [2013] explored similar nonseasonal OcM fluctuations in the Mediterranean Sea and attributed them to concurrent wind stress anomalies in the subtropical North Atlantic. The Arctic Ocean has a number of oceanographic features reminiscent of the Mediterranean Sea. Albeit larger, the Artic Ocean is also a semienclosed basin with a narrow and shallow gateway to the Pacific Ocean at the Bering Strait, and with a far less restricted exchange with the Atlantic Ocean through the Fram Strait and the Barents Sea. Therefore, we hypothesize that forcing mechanisms driving the nonseasonal OcM fluctuations in the Arctic Ocean are possibly similar to the Mediterranean.

2. Data and Methods

2.1. Ocean Mass From GRACE

[7] The GRACE twin-satellites have observed time variations of the Earth's gravity field since May 2002 and provide unique measurements of large-scale ocean mass changes. We use the GRACE Release-05 monthly bottom pressure anomalies based on spherical harmonics from the Geoforschungzentrum Potsdam (GFZ RL 5.0), which we refer to as OcM. The GRACE data are mapped on a 1° × 1° grid and distributed via GRACE Tellus web resource (http://grace.jpl.nasa.gov). Details on data processing can be found in *Chambers and Bonin* [2012]. While the results presented in this manuscript are based on GFZ RL 5.0 product, similar results are obtained with the University of Texas Center for Space Research (CSR RL 5.0) product.

[8] The Arctic OcM data are used over the geographical domain bounded by 65°N in the south, so that the data include the Arctic Ocean and the adjacent basins of the North Atlantic (Baffin Bay, Norwegian, and Greenland seas). Using the *Wahr et al.* [2006] approach, which essentially assumes that short-period signals are noise, we obtain thermore, we subtract a monthly mean climatology and a linear trend to focus on the nonseasonal time scales. From these OcM anomalies, we calculate horizontal geostrophic velocity anomalies to analyze associated changes in the large-scale ocean circulation. Note that due to recent battery management issues since 2011, the GRACE instruments are periodically turned off for periods of up to 4 weeks at approximately 6 month intervals. For the following comparisons of OcM to wind stress, we linearly interpolate the missing GRACE months. This means that rapid OcM fluctuations that may occur during missing months may not be recovered properly.

2.2. Atmospheric Data

[10] The observed OcM variability is coupled to monthly mean surface wind stress data obtained from the ECMWF Re-Analysis (ERA-Interim, www.ecmwf.net) [*Dee et al.*, 2011]. We use wind stress data over the circumpolar domain bounded by 50°N in the south. This is larger than the domain used for the OcM data, because the Arctic OcM can be correlated with wind forcing beyond the Arctic Ocean boundary. To focus on the nonseasonal fluctuations, the monthly mean climatology was subtracted, as was done for the OcM data. In addition, we use the monthly Arctic Oscillation (AO) index distributed by NOAA's National Weather Service Climate Prediction Center (http://www.cpc.ncep.noaa.gov).

2.3. ECCO2 Ocean Data Synthesis

[11] To compare with and analyze the observed nonseasonal OcM variability, we use a high-resolution (18 km grid spacing) ECCO2 (Estimating the Circulation and Climate of the Ocean, Phase II) ocean data synthesis product (www.ecco2.org), which is obtained by a least squares fit of a global full-depth-ocean and sea-ice configuration of the Massachusetts Institute of Technology general circulation model (MITgcm) [*Marshall et al.*, 1997] to selected satellite and in situ data. The MITgcm includes a dynamic/thermodynamic sea-ice model [*Losch et al.*, 2010]. The simulations are forced by the Japanese 25 year Re-Analysis (JRA-25; http://jra.kishou.go.jp/JRA-25/) [*Onogi et al.*, 2007] and constrained by observations using the model Green's function to adjust a series of empirical control parameters [*Menemenlis et al.*, 2005]. Observational constraints include satellite altimetry SSH, sea surface temperature, vertical temperature, and salinity profiles, and sea-ice concentrations, motion, and thickness. The control parameters include initial hydrography, atmospheric boundary conditions, and background vertical diffusivity. The ECCO2 solutions are com-

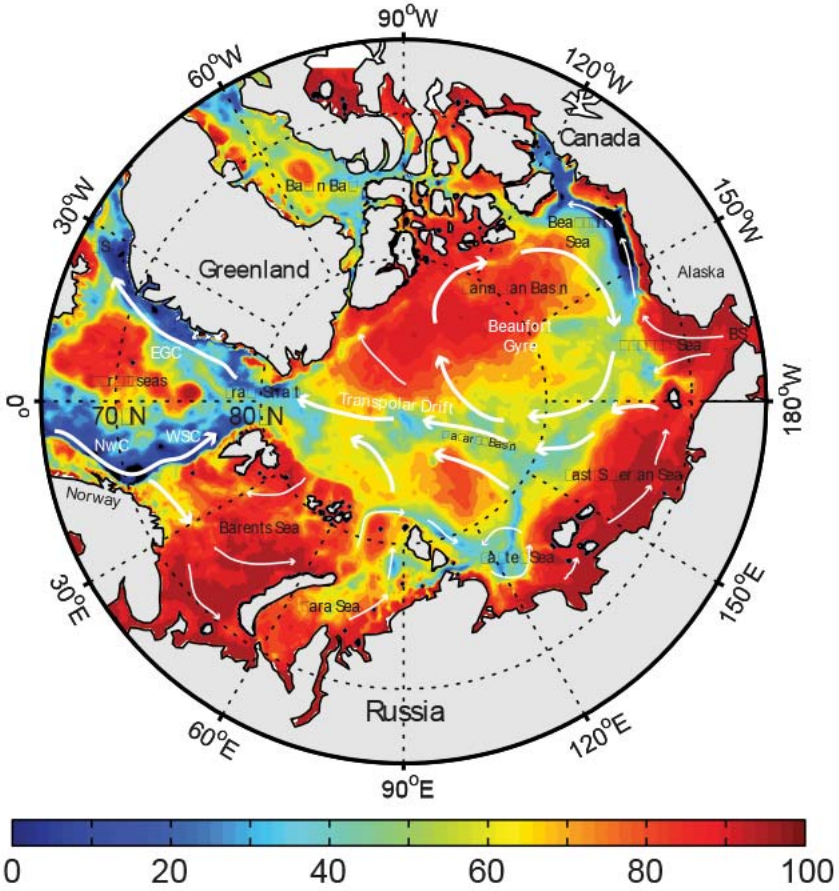

Figure 1. Portion (%) of the nonseasonal sea surface height variance explained by the nonseasonal OcM in ECCO2 model. White arrows show the general upper-ocean circulation pattern. Abbreviations: NwC—Norwegian Current, WSC—West Spitsbergen Current, EGC—East Greenland Current, BS—Bering Strait, DS—Denmark Strait.

computed by fitting harmonic functions with corresponding frequencies in a least squares sense. The net lateral transports are computed from horizontal velocities across the 65°N circumpolar section and across its segments in the North Atlantic and Bering Strait.

2.4. Identification of Coupled Fields

[13] To evaluate the temporally covarying, but not necessarily spatially colocated signals in OcM and wind stress fields, we use a coupled Empirical Orthogonal Functions

60. This means that correlation coefficients above 0.25 are significant at 95% confidence level.

3. Results

3.1. Arctic Ocean Mass Changes From GRACE and ECCO2

[14] The analysis of the ECCO2-simulated SSH and OcM indicates that the nonseasonal SSH variability in the Arctic Ocean is mostly mass related (Figure 1). The non-

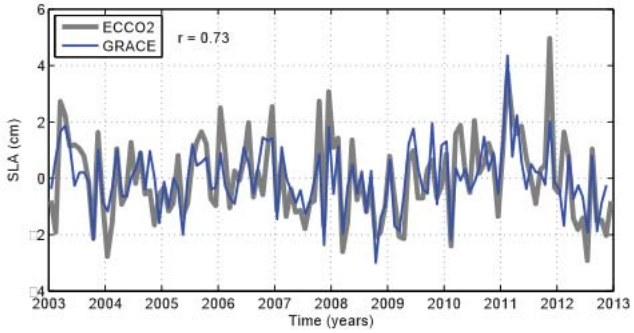

Figure 2. The basin-averaged nonseasonal OcM from GRACE (blue) and from ECCO2 model (gray). Note that the large signal in November 2011 is likely real, but was not observed with GRACE due to an instrument outage between November 17 and December 12. Accounting for this outage, largely removes the peak from the model estimate. For a monthly GRACE-OcM estimate, the 1-sigma uncertainty is about 9 mm, based on *Wahr et al*. [2006].

[15] The area-averaged nonseasonal OcM from GRACE exhibits variability with a standard deviation of about 1 cm (Figure 2). This value is greater than the annual OcM amplitude (about 0.7 cm), estimated by a harmonic analysis. There is a good agreement between the GRACE-observed and ECCO2-simulated nonseasonal OcM in the Arctic Ocean with correlation of 0.73 (Figure 2). Most short-term OcM fluctuations are well reproduced by the model. What is important for the objectives of this study is that the observed high anomaly in February 2011 is well simulated by ECCO2. The timing and the amplitudes of the observed and simulated anomalies are almost identical, indicating that ECCO2 can be used to investigate the mechanisms responsible for the observed nonseasonal OcM fluctuations.

[16] The largest discrepancy between GRACE and ECCO2 OcM was in November 2011. This discrepancy can be explained by a partial GRACE instrument outage between November 17 and December 12. In addition, the November 2011 GRACE monthly solution is actually derived from observations between October 16 and November 16. Introducing the gap and resampling the 3 day ECCO2 OcM time series at the GRACE epoch reduces the apparent misfit between the model and observations for this particular event by about 2 cm (not shown). Therefore, the November 2011 peak simulated by ECCO2 is likely to be a real OcM anomaly.

located in the Arctic interior and the other over the Russian continental shelf. The absolute correlation between the PC-1 of τ_x and OcM in these areas exceeds 0.5. The corresponding wind stress pattern (Figure 3b) has two maxima, located over the northeastern North Atlantic and over the Kara, Laptev, and East-Siberian seas with absolute correlations above 0.4. The time evolution of these spatial patterns (Figure 3c) indicates that when the zonal wind between about 70°N–85°N and 60°E–210°E intensifies/reduces, OcM rises/falls over the Russian shelf seas and falls/rises in the central Arctic, which is consistent with Ekman dynamics. An intensification/reduction of westerly winds around 60°N in the North Atlantic also leads to an increased/decreased southward Ekman transport that is correlated with a decrease/increase of OcM in the Nordic seas and in the central Arctic. The dipole oscillation pattern in Figure 3a corresponds to the second EOF of bottom pressure from *Peralta-Ferriz* [2012] and *Peralta-Ferriz et al.* [2013], forced by changes in atmospheric pressure over the central Arctic and east Greenland that drive zonal winds. The zonal wind anomalies over the Arctic Ocean are related to the Arctic Oscillation (AO) (Figure 3c). The correlation coefficient between the PC-1 of τ_x and the AO index is 0.52, while the correlation between the PC-1 of OcM and the AO index is 0.28. The positive/negative AO index corresponds to lower/higher than average sea level pressure at the North Pole and, in turn, to stronger/weaker westerly winds. The low AO index in 2010 was associated with an OcM decrease over the Russian shelf seas and an OcM increase over the central Arctic.

[19] The coupled OcM/τ_y mode reveals a basin-wide coherent pattern of OcM changes, with the exception of the shallow areas of the Kara, Laptev, and East Siberian seas (Figure 4a). The correlation between the PC-1 of τ_y and OcM over most of the Arctic Ocean is well above 0.5. The PC-1 time series (Figure 4c) demonstrate that this is the mode that describes the basin-averaged fluctuations of OcM shown in Figure 2. The correlation between the PC-1 of OcM and τ_y is 0.96, while the correlation between the PC-1 of OcM and the basin-averaged OcM is 0.65. The record-high OcM value observed in February 2011 (Figure 2) is well represented by the coupled PC-1 of OcM and τ_y. The basin-coherent mode corresponds to the first EOF of bottom pressure forced by an atmospheric pressure dipole that straddles the Nordic seas from *Peralta-Ferriz* [2012] and *Peralta-Ferriz et al.* [2013]. We note that the basin-coherent OcM fluctuations are correlated with the meridional wind over the northeastern North Atlantic, the Nordic seas, and over the Bering Sea (Figure 4b). Thus, an intensi-

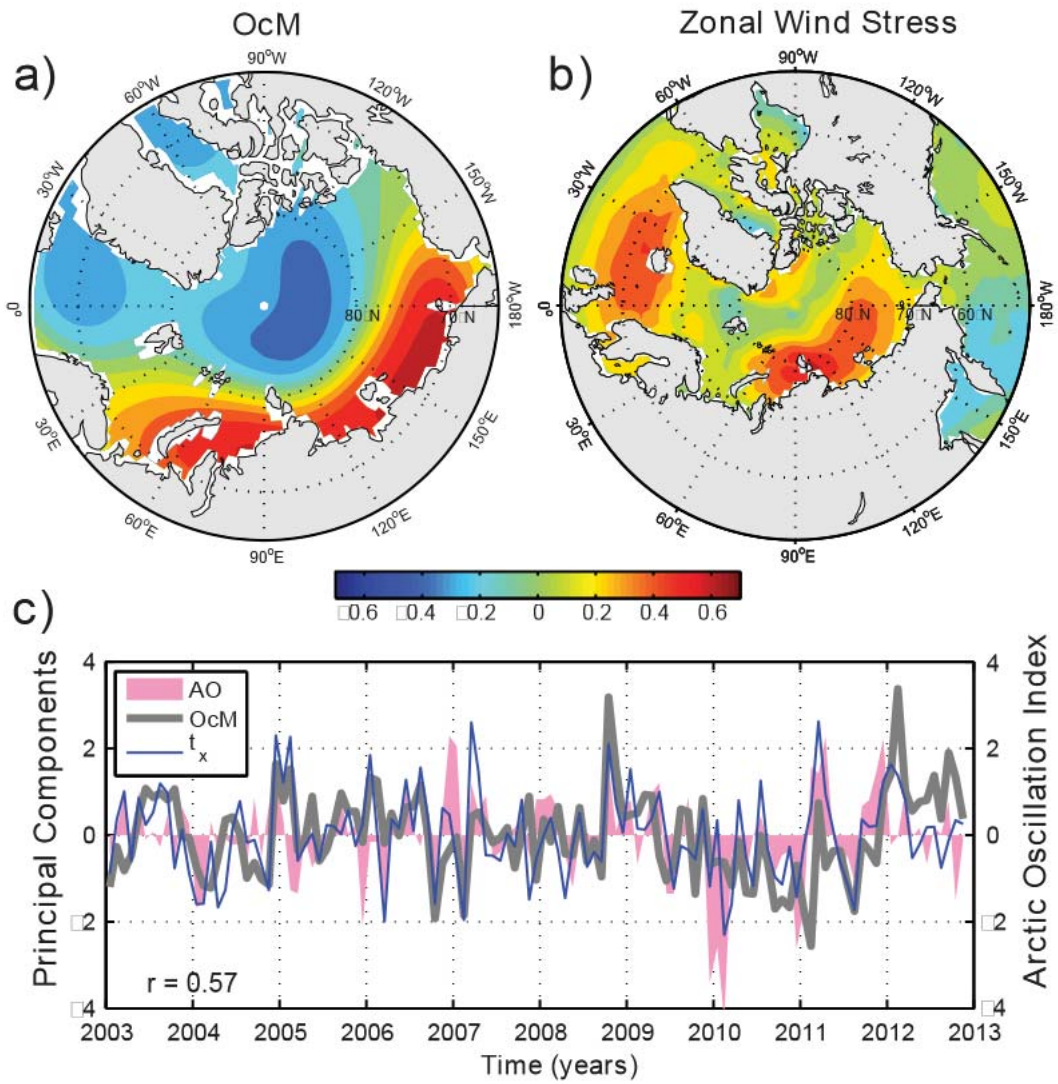

Figure 3. (a and b) The spatial patterns and (c) the principal component (PC) time series of the first coupled EOF of the Arctic OcM and zonal wind stress (τ_x). The spatial patterns are shown as heterogeneous correlation maps: (Figure 3a) the correlation between the PC-1 of τ_x and OcM field and (Figure 3b) the correlation between the PC-1 of OCM and τ_x field. The Arctic Oscillation index is shown by the pink-shaded area in Figure 3c plot.

OcM anomalies, we plot the 10 m wind speed anomaly, wind stress curl anomaly, and oceanic geostrophic velocity anomaly vectors averaged over the periods when the basin-mean OcM anomalies (in Figure 2) are larger than ± 1 cm. The southward/northward wind anomalies over the Nordic

et al., 2004]. At Bering Strait, when it is ice free, the along-strait wind is likely to modulate the inflow into the Arctic Ocean, similar to how wind affects transport across the Strait of Gibraltar and hence the Mediterranean sea level [*Fukumori et al.*, 2007; *Landerer and Volkov*, 2013]. The

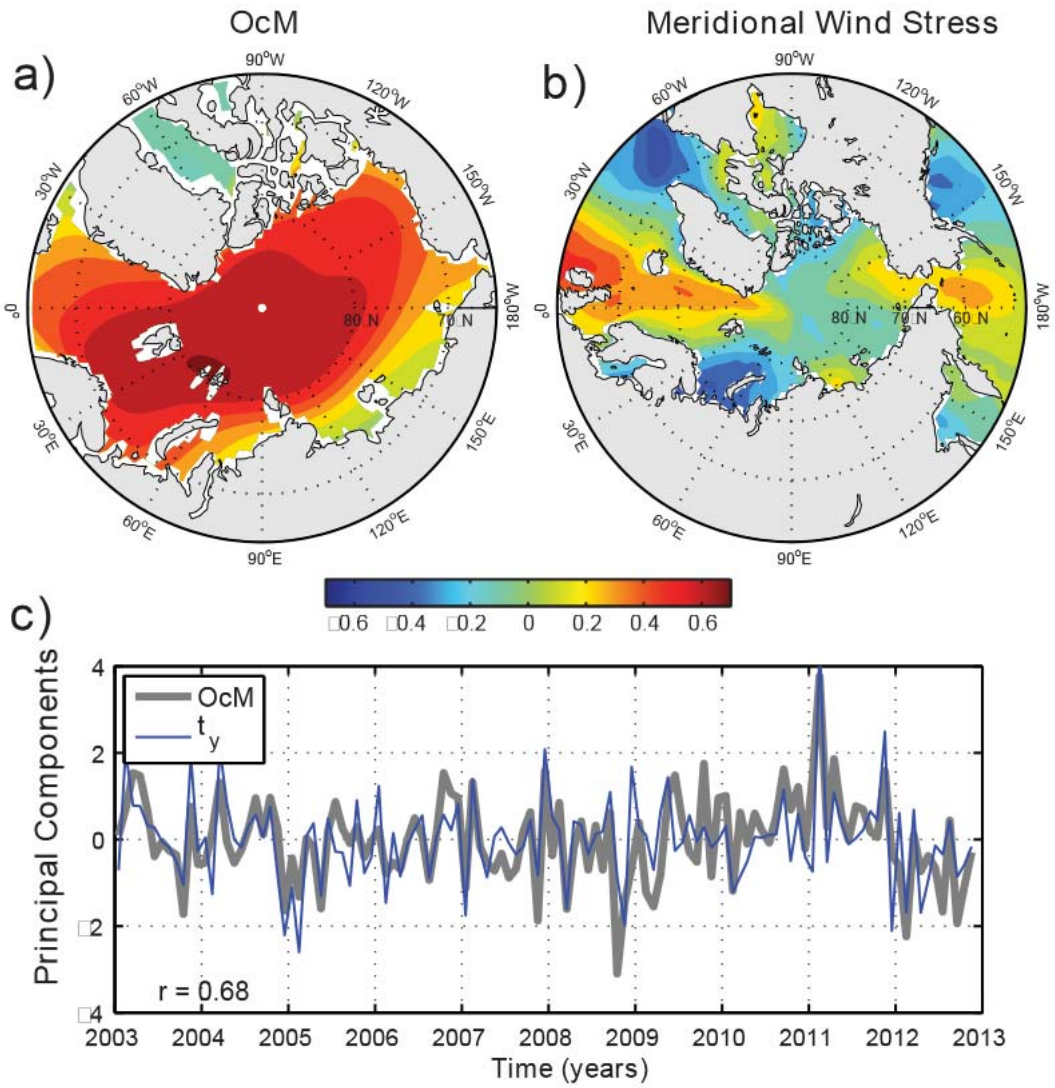

Figure 4. (a and b) The spatial patterns and (c) the principal component (PC) time series of the first coupled EOF of the Arctic OcM and meridional wind stress (τ_y). The spatial patterns are shown as heterogeneous correlation maps: (Figure 4a) the correlation between the PC-1 of τ_y and OcM field and (Figure 4b) the correlation between the PC-1 of OcM and τ_y field.

transport is questionable, because the meridional gradient of planetary vorticity (beta) is weak at high latitudes and topographic effects are particularly important [*N□st and Isachsen*, 2003]. The results of our study demonstrate that during the low/high Arctic OcM anomalies the wind stress mass transport of wind-driven currents. Therefore, during the low/high Arctic OcM anomalies there should be wind-driven southward/northward transport anomalies over this part of the North Atlantic that hypothetically can lead to outflow/inflow anomalies from/to the Nordic seas. The

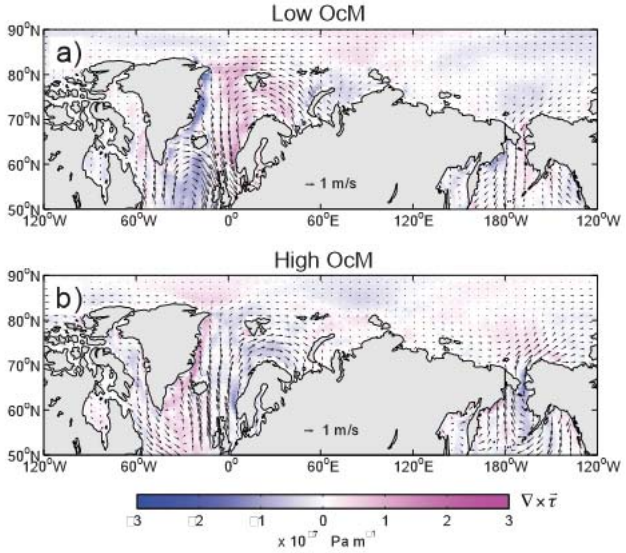

Figure 5. The 10 m height wind vectors and wind stress curl (color) averaged over the period of (a) low and (b) high OcM anomaly, i.e., when OcM in Figure 2 is less than −1 cm and greater than 1 cm, respectively.

variations [*Ponte et al.*, 2007; *Dobslaw and Thomas*, 2007; *Peralta-Ferriz and Morison*, 2010]. What, in particular, caused the large anomalies in February of 2011 and in November 2011?

[24] The time change of the basin-averaged OcM is compensated by the lateral volume transport and fresh water fluxes (precipitation, evaporation, and river runoff) (Figure 7a). The rate of OcM change due to fresh water fluxes (red curve) is mostly positive. Any pressure buildup in the Arctic Ocean due to fresh water input would quickly propagate away to the rest of the World Ocean. Although wind forcing may act to retain fresh water in the basin by reducing the compensating outflow, as occurs at the seasonal time scale [*Dobslaw and Thomas*, 2007; *Peralta-Ferriz and Morison*, 2010], the nonseasonal OcM variability is not significantly affected by fresh water retained in the basin. The variability of the basin-averaged nonseasonal OcM is mostly determined by the net transport across 65°N (Figure 7a, blue curve).

[25] The observed record-high anomaly at the beginning of 2011 is the result of the net transport anomalies across 65°N. There were several relatively prolonged events with positive transport anomalies into the Arctic in winter 2010/2011 (Figure 7a). Using the model, we separate the net sector transport (Figure 7b). The correlation between the total transport and the Atlantic sector transport is 0.77, while the correlation between the total transport and the Bering Strait transport is not significant (0.17).

[26] To investigate the relative contributions to the record-high OcM anomalies in February and November 2011, we compute the detrended cumulative sums of the net Atlantic sector and Bering Strait transports, scale them by the Arctic Ocean area and multiply by the model time interval (3 days) to obtain the equivalent OcM time series (Figure 8, note that the tick marks of x-axis correspond to midmonth dates). The OcM anomaly in February 2011 was mostly due to a positive anomaly of the Atlantic sector transport. At the same time, the Atlantic transport anomaly was not compensated by a sizable reduction in the Bering Strait inflow. On the contrary, the Bering Strait inflow increased about 2 weeks later, leading to a further Arctic OcM increase. In fact, the Arctic OcM reached its maximum value at the end of February with approximately equal contributions from Atlantic and Pacific inflows (Figure 8). The OcM anomaly in November 2011 was initiated by a stronger than average inflow through the Bering Strait in the second half of October followed by an inflow anomaly from the Atlantic Ocean. Thus, although the variability of the Arctic OcM is mostly due to the Atlantic sector transport anomalies, both the Atlantic and Pacific gateways can be equally important for generating large Arctic OcM anomalies.

[27] The ECCO2 atmospheric circulation patterns associated with February and November 2011 OcM anomalies (Figure 9) are characterized by northward anomalies over the Nordic and Barents seas and positive wind stress curl anomalies in the North Atlantic south of 65°N (similar to Figure 5b). Unlike the Fram Strait, where sea ice is relatively free to move, near the narrow and shallow Bering Strait, winter sea ice is constrained by interaction with land and bottom and can attenuate the transfer of momentum to the water. However, strong northward wind anomalies over

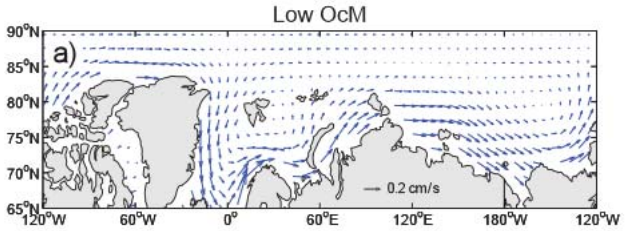

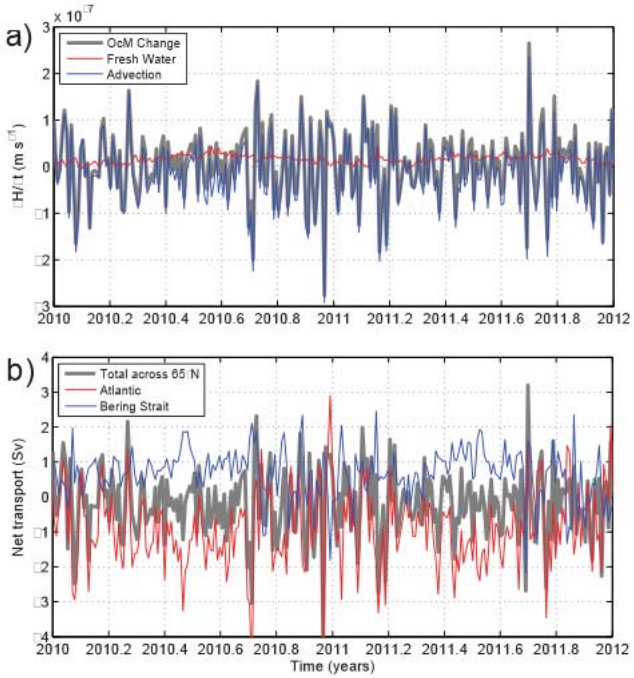

Figure 7. (a) The time change of the Arctic OcM (gray), the net transport across 65°N scaled by the ocean area north of this latitude (blue), and fresh water fluxes (red); (b) net transport in Sverdrups (1 Sv = 10^6 m^3 s^{-1}): total across 65°N (gray), across 65°N in the Atlantic Ocean (red), and through the Bering Strait (blue).

the Bering Sea were able to force water into the Arctic Ocean in February 2011, when the area with the concentration of sea ice over 50% extended south to about 60°N (blue curve in Figure 9, left). The Bering Strait throughflow increased in the second half of February and remained high through March, but in March it was already compensated by an outflow through the Atlantic sector (Figure 8). Because of the possible effect of sea ice in the northern part of the Bering Sea, the mechanism here is therefore different from direct forcing by the along-strait wind as occurs in the Mediterranean Sea [*Fukumori et al.*, 2007; *Landerer and Volkov*, 2013]. We suggest that a likely mechanism is related to Ekman dynamics: the northward wind anomalies over the Bering Sea reduce the strength of the southward Kamchatka Current and intensify the northward Bering Slope Current along the Alaska continental shelf, part of which eventually supplies water to the Bering Strait

urements exhibited a record-high anomaly of about 4 cm above the 2003–2012 average in February 2011.

[29] Coupling satellite measurements of OcM with wind stress, we have found that the zonal wind pattern is correlated with a dipole pattern of OcM change (Figure 3). When westerly winds intensify/reduce over the North Atlantic at about 60°N and over the Russian continental shelf break, OcM decreases/increases in the Nordic seas and in the central Arctic, and increases/decreases over the Russian Arctic shelf, consistent with Ekman dynamics. The time evolution of this pattern is related to the AO index.

[30] The basin-wide OcM changes in the Arctic Ocean are correlated with the northward wind near its gateways: low/high OcM anomalies in the Arctic Ocean are associated with northward wind anomalies over the northeastern North Atlantic and Nordic seas, and over the Bering Sea (Figure 4). This variability pattern is responsible for the record-high anomaly observed in February 2011. We conclude that the meridional wind anomalies over the Nordic seas can modulate the strength of the East Greenland and West Spitsbergen currents, and eventually the transport across the Fram Strait, via Ekman dynamics. The low/high Arctic OcM anomalies correspond to the negative/positive anomalies of the wind stress curl over the North Atlantic, just south of 65°N (Figure 5). This suggests that associated anomalies in Sverdrup transport can influence the southern boundary of the Nordic seas and, thus, be one of the possible mechanisms for the wind-driven nonseasonal fluctuations of the Arctic OcM. Demonstrating the great utility of the GRACE observations, we have also revealed associated changes in the large-scale ocean circulation. The cyclonic/anticyclonic circulation anomaly with an anomalous outflow/inflow through the Fram Strait is associated with the low/high Arctic OcM (Figure 6).

[31] The basin-wide fluctuations of OcM and the record-high anomaly in particular, are well simulated by the ECCO2 model. The model also simulated a somewhat larger anomaly in November 2011, which is likely to be real, but not resolved by GRACE due to an instrument shutdown at around the same time. Based on ECCO2 model output, we conclude that the contribution of fresh water fluxes is negligible on nonseasonal time scales, and most of the OcM variability is explained by the net horizontal

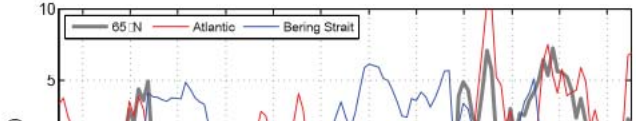

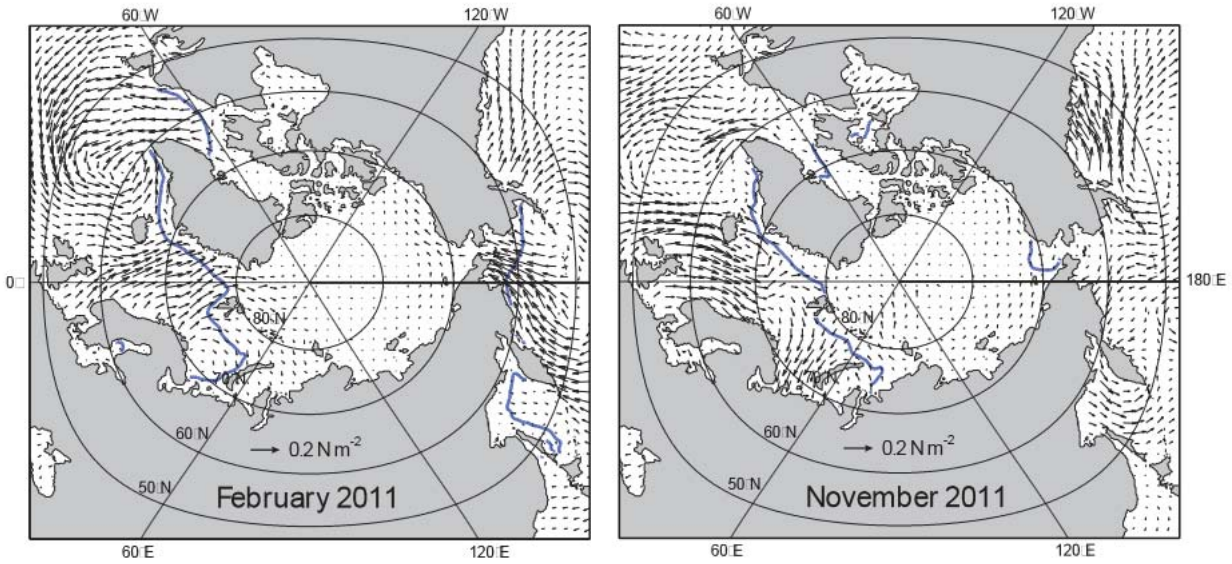

Figure 9. The ECCO2 February and November 2011 wind stress anomaly vectors, obtained by subtracting the monthly mean climatology fields. North of the blue boundary, the fractional ice covered area of grid cells exceeds 50%.

transports that mostly represent the wind-driven redistribution of water (Figure 7a).

[32] Although the Bering Strait transport usually compensates for the Atlantic transport anomalies, most of the variability of the Arctic OcM is driven by the variability of noncompensated transport across the Atlantic sector (Figure 7b). However, we have shown that the contribution of the Bering Strait transport was significant for both of the large Arctic Ocean mass anomalies in February and in November of 2011, when it did not compensate for the Atlantic transport anomalies (Figure 8). We suggest that during winter months, when the shallow northern part of the Bering Sea is covered with sea ice, the northward wind anomalies by the means of Ekman transport can affect the strength of the Kamchatka and the Bering Slope currents and lead to the divergence or convergence of water in the northern part of the Bering Sea, which controls the net transport across the Bering Straight.

[33] **Acknowledgments.** The ECCO2 model runs have been carried out at Jet Propulsion Laboratory, California Institute of Technology (http://ecco2.jpl.nasa.gov). GRACE ocean data were processed by Don P. Chambers, supported by the NASA MEASURES Program, and are available at http://grace.jpl.nasa.gov. The authors thank James Morison,

Calafat, F. M., D. P. Chambers, and M. N. Tsimplis (2013), Interannual to decadal sea level variability in the coastal zones of the Norwegian and Siberian seas: The role of atmospheric forcing, *J. Geophys. Res.*, *118*, 1287–1301, doi:10.1002/JGRC.20106.

Chambers, D. P., and J. A. Bonin (2012), Evaluation of Release 05 time-variable gravity coefficients over the ocean, *Ocean Sci.*, *8*, 859–868, doi: 10.5194/os-8–859-2012.

Dee, D. P., et al. (2011), The ERA-Interim reanalysis: configuration and performance of the data assimilation system, *Q. J. R. Meteorol. Soc.*, *137*, 553–597.

Dobslaw, H., and M. Thomas (2007), Impact of river run-off on global ocean mass redistribution, *Geophys. J. Int.*, *168*(2), 527–532, doi: 10.1111.j.1365-246X.2006.03247.x.

Fukumori, I., D. Menemenlis, and T. Lee (2007), A near-uniform basin-wide sea level fluctuation of the Mediterranean Sea, *J. Phys. Oceanogr.*, *37*(2), 338–358.

Landerer, F. W., and D. L. Volkov (2013), The anatomy of recent large sea level fluctuations in the Mediterranean Sea, *Geophys. Res. Lett.*, *40*, 553–557, doi:10.1002/GRL.50140.

Losch, M., D. Menemenlis, P. Heimbach, J.-M. Campin, and C. Hill (2010), On the formulation of sea-ice models. Part 1: effects of different solver implementations and parameterizations, *Ocean Modeling*, *33*, 129–144.

Marshall, J., A. Adcroft, C. Hill, L. Perelman, and C. Heisey (1997), A finite volume, incompressible Navier-Stokes model for studies of the ocean on parallel computers, *J. Geophys. Res.*, *102*, 5753–5766.

Menemenlis, D., I. Fukumori, and T. Lee (2005), Using Green's functions to calibrate an Ocean General Circulation model, *Mon. Weather Rev.*, *133*, 1224–1240.

Onogi, K., et al. (2007), The JRA-25 Reanalysis, *J. Meteorol. Soc. Jpn.*, *85*, 369–432.

Peralta-Ferriz, C., J. H. Morison, J. M. Wallace, J. A. Bonin, J. Zhang (2013), Arctic Ocean circulation patterns revealed by GRACE, in press, doi:10.1175/JCLI-D-13-00013.1.

Peralta-Ferriz, C. (2012), Arctic Ocean circulation patterns revealed by ocean bottom pressure anomalies, PhD thesis, Univ. of Wash., Seattle, Wash.

Peralta-Ferriz, C., and J. Morison (2010), Understanding the annual cycle of the Arctic Ocean bottom pressure, *Geophys. Res. Lett.*, *37*, L10603, doi:10.1029/2010GL042827.

Peralta-Ferriz, C., J. H. Morison, J. M. Wallace, and J. Zhang (2011), A basin-coherent mode of sub-monthly variability in the Arctic Ocean, *Geophys. Res. Lett.*, *38*, L14606, doi:10.1029/2011GL048142.

Ponte, R. M., K. J. Quinn, C. Wunsch, and P. Heimbach (2007), A comparison of model and GRACE estimates of the large-scale seasonal cycle in ocean bottom pressure, *Geophys. Res. Lett.*, *34*, L09603, doi:10.1029/2007GL029599.

Proshutinsky, A., I. M. Ashik, E. N. Dvorkin, S. Hakkinen, R. A. Krishfield, and W. R. Peltier (2004), Secular sea level change in the Russian sector of the Arctic Ocean, *J. Geophys. Res.*, *109*, C03042, doi:10.1029/2003JC002007.

Proshutinsky, A., I. Ashik, S. Hākkinen, E. Hunke, R. Krishfield, M. Maltrud, W. Maslowski, and J. Zhang (2007), Sea level variability in the Arctic Ocean from AOMIP models, *J. Geophys. Res.*, *112*, C04S08, doi:10.1029/2006JC003916.

Richter, K., J. E. [. Nilsen, and H. Drange (2012), Contributions to sea level variability along the Norwegian coast for 1960–2010, *J. Geophys. Res.*, *117*, C05038, doi:10.1029/2011JC007826.

Schauer, U., E. Fahrbach, S. Osterhus, and G. Rohardt (2004), Arctic warming through the Fram Strait: Oceanic heat transport from 3 years of measurements, *J. Geophys. Res.*, *109*, C06026, doi:10.1029/2003JC0011823.

Serreze, M. C., A. P. Barrett, A. G. Slater, R. A. Woodgate, K. Aagaard, R. B. Lammers, M. Steele, R. Moritz, M. Meredith, and C. M. Lee (2006), The large-scale freshwater cycle of the Arctic, *J. Geophys. Res.*, *111*, C11010, doi:10.1029/2005JC003424.

Steele, M., and W. Ermold (2007), Steric sea level change in the Northern seas, *J. Clim.*, *20*, 403–417.

Tapley, B. D., S. Bettadpur, J. R. Ries, P. F. Thompson, and M. M. Watkins (2004), GRACE measurements of mass variability in the Earth systems, *Science*, *305*, 503–505.

Volkov, D. L., and M.-I. Pujol (2012), Quality assessment of a satellite altimetry data product in the Nordic, Barents, and Kara seas, *J. Geophys. Res.*, *117*, C03025, doi:10.1029/2011JC007557.

Volkov, D. L., T. V. Belonenko, and V. R. Foux (2013a), Puzzling over the dynamics of the Lofoten Basin—A sub-Arctic hot spot of ocean variability, *Geophys. Res. Lett.*, *40*, 738–743, doi:10.1002/GRL.50126.

Volkov, D. L., F. W. Landerer, and S. A. Kirillov (2013b), The genesis of sea level variability in the Barents Sea, *Cont. Shelf Res.*, *66*, 92–104, doi:10.1016/j.csr.2013.07.007.

von Storch, H., and F. W. Zwiers (1999), *Statistical Analysis in Climate Research*, Cambridge Univ. Press, Cambridge, U. K.

Wahr, J., S. Swenson, and I. Velicogna (2006), Accuracy of GRACE mass estimates, *Geophys. Res. Lett.*, *33*, L06401, doi:10.1029/2005GL025305.